



## Supplementary Materials for

### **The Yellowstone magmatic system from the mantle plume to the upper crust**

Hsin-Hua Huang,\* Fan-Chi Lin, Brandon Schmandt, Jamie Farrell, Robert B. Smith,  
Victor C. Tsai

\*Corresponding author. E-mail: [hsinhua.huang@utah.edu](mailto:hsinhua.huang@utah.edu)

Published 23 April 2015 on *Science Express*  
DOI: 10.1126/science.aaa5648

**This PDF file includes:**

Materials and Methods

Figs. S1 to S7

Tables S1 to S3

References

## Materials and Methods

### Seismic tomographic methods and model parameterization

A recently developed code for multi-dataset tomographic joint inversion is employed in this study (23, 34-36), in which the absolute travel-time residuals from local earthquake data and the relative travel-time residuals from teleseismic data are simultaneously minimized. For the travel-time calculation, we used the modified pseudobending method in three-dimensional (3-D) spherical coordinates (37, 38), and retraced the local and teleseismic rays after each iteration with a nonlinear approximation. The 3-D velocity model is parameterized with a spatial grid of 15 km in longitude and latitude and incremental depth nodes from -10 to 160 km as shown in Table S1. The initial 1-D  $P$ -wave velocity ( $V_P$ ) model follows the ak135 global 1-D model (39) but employs a local 1-D model (3) for the shallowest 20-km depth (Table S1).

Since the number of local earthquake absolute  $P$ -wave arrival times is 10 times more than the teleseismic differential arrival time dataset, these two datasets should not be weighted equally. However, in this study we weighted both types of data equally but decoupled their mutual influence with a two-step approach (23). We inverted the local earthquake data for a 3-D  $P$ -wave crustal model first, and then used the resulting 3-D model as an initial model for the joint inversion of both local and teleseismic data in the second step. In this way, the residuals of local seismic data have been reduced as much as possible in the first inversion and do not dominate the following joint inversion. After 8 iterations (4 with local earthquake data alone and 4 with joint inversion), the total residual RMS decreases from 0.282 to 0.134 s, a 52% reduction. Fig. S1 shows that all station residuals are reduced significantly after the two-step inversion. By extensively testing the regularization parameters, a damping factor of 40 and a smoothing factor of 30 were chosen for the final analyses (Fig. S2).

Because the Yellowstone local earthquake data set (3) is used in this study, the upper-crustal low velocity body (LVB) in our model is very similar to that of (3) in geometry but is greater in size and anomaly magnitude. The greater size and magnitude may mainly arise from differences in coordinates and ray tracing methods between our code and the open-source program *simulps14* used in (3). The spherical coordinates we used tend to trace shorter paths than the flattened Cartesian coordinates do, and in turn require slower low velocity anomalies to compensate for the shorter/faster path. The coordinate effect would be more significant for the teleseismic data on a scale of over 200 km (40). In this sense, rather than using the existing local model of (3), it is also better to re-invert the local earthquake data in spherical coordinates to achieve consistency with the teleseismic data.

### Resolution tests with checkerboard and characteristic models

We conducted conventional seismic tomography checkerboard tests and characteristic-model synthetic tests for resolution assessment. In the checkerboard test, we input a checkerboard-like model with -5% and 5% variations in  $P$ -wave velocity ( $V_P$ ), interchanging two nodes at a time horizontally and three nodes at a time vertically except for the top two nodes. Results show generally good recovery at each depth slice (Fig. S3). Velocity variations between 8 and 14 km, 35 and 50 km, and 100 and 130 km are resolved relatively poorer compared to other depths because the velocities there vary sharply in three dimensions rather than primarily laterally as in the other depth slices.

A characteristic model was designed according to the model images we obtained in Fig. 3, with four prominent low velocity anomalies (LVA). The LVAs at 4-14 and 20-40 km represent the upper and lower magma reservoirs, and the other two deep LVAs represent the plume-like feature and localized mantle velocity anomaly to the northwest and southeast of the caldera (Fig. S4). Performing inversions using local data alone, teleseismic data alone, and with both types of data, the results clearly demonstrate the capability of the joint inversion to resolve the entire crustal magmatic system. The results also show the robust nature of the separation between the two LVAs in the crust. However, because of a smearing effect caused by the similar incident angles of sub-vertical teleseismic incoming rays, the bottom of the lower-crustal LVA is smeared downward to connect with the plume anomaly, as we saw in the real data inversion (Fig. 3C). This similarity implies that the bottom of the lower crustal reservoir is possibly shallower than imaged in our model. Thus, this reservoir likely lies within the crust, i.e., above ~45 km in the Yellowstone area (26) as shown in Fig. 4. The results of another negative test of a characteristic model without the lower-crustal LVA are also displayed in Fig. S5, confirming that the existence of a lower-crustal LVA is resolvable and robust although a slight smearing anomaly in the lower crust is present.

To further test how noise in the data causes smearing, we introduced random noise centered at 0 s with a standard deviation of 0.13 s (based on the RMS travel time residuals of the final real-data inversion) into the synthetic travel times (Fig. S6). The results show that the smearing at the bottom of the lower-crustal LVB and some streaking artifacts are enhanced (indicated by black arrows); however, the main features we interpret clearly remain and are not likely due to data noise.

### Resolvability index translation

Based on the results of the checkerboard test, we translated the model recovery level into a resolvability index,  $R$  (36, 41), which is defined as

$$R = \frac{\sum_{i=i-n}^{i+n} \sum_{j=j-n}^{j+n} \sum_{k=k-n}^{k+n} (Vt_{i,j,k} + Vr_{i,j,k})^2}{2 \sum_{i=i-n}^{i+n} \sum_{j=j-n}^{j+n} \sum_{k=k-n}^{k+n} (Vt_{i,j,k}^2 + Vr_{i,j,k}^2)} \quad (S1)$$

where  $Vt$  are the true velocities (i.e., from a known synthetic model) and  $Vr$  are the recovered velocities at nodes denoted by indices  $i, j, k$  in 3-D space. This resolvability factor is then operated over a defined range by a desired number of nodes,  $n$ . A larger value of  $n$  produces a smoother map and vice versa. We chose  $n = 5$  in this case, which is slightly larger than the perturbation wavelength ( $n = 3$ ) in the checkerboard test and generally produces good results.  $R$  ranges from 0 to 1, in which  $R = 1$  represents the velocity anomaly is 100% recovered (nodes with significant ray crossing),  $R = 0.5$  indicates 0% recovered (nodes with no rays crossing), and  $R = 0$  denotes a velocity that is -100% perturbed (unstable inversion nodes). The corresponding  $R$  index and the derivative weighted sum (DWS) (42) map at different depths are also shown in Fig. S3. The DWS at each velocity model node can be viewed as a proxy for the ray density. Compared to the recovery of the checkerboard tests,  $R = 0.6$  is considered a reasonable lower bound for a resolvable area (36).  $R$  is therefore used as an index to shade areas with values smaller than 0.6 as in Fig. 2 and 3.

### Estimate of Fresnel zone widths

Following the derivation (43) in a 3-D homogenous medium, a simplified calculation of a Fresnel zone width,  $f$ , is as follows:

$$f = 2 \left[ \frac{\lambda d(L-d)}{L} \right]^{\frac{1}{2}} \quad (\text{S2})$$

where  $\lambda$  is the wavelength,  $L$  is the total distance between source and receiver, and  $d$  is the distance from the source or receiver. Given the 1-s period of teleseismic  $P$ -waves used and the  $\sim 6$  km/s average crustal  $V_P$ , the wavelength of a teleseismic wave is 6 km. Using the *Taup* toolkit (44) with the *ak135* global 1-D model (39) for a distance range of  $30^\circ$  to  $90^\circ$ , the length of the ray path,  $L$ , is calculated to be  $\sim 3,600$  and  $\sim 11,350$  km for the  $30^\circ$  and  $90^\circ$  epicentral distances of the teleseismic data, respectively. For an example lower-crustal LVB at 20-40 km, assuming  $d$  is 30 km from the receiver, we will then have a Fresnel zone width of  $\sim 27$  km for either the shortest ( $30^\circ$ ) or the longest ( $90^\circ$ ) epicentral distances. This calculation shows that the 1-s teleseismic  $P$ -wave data that we used in the study are able to resolve any structure with a radius larger than  $\sim 27$  km, for which the imaged lower-crustal LVB is much larger. However, considering the typical dimensions observed at field outcrops, the volcanic dikes inferred to exist between the two crustal LVBs cannot be detected seismically in this case.

### Velocity anomalies caused by temperature

Granite and the mafic granulite are widely accepted as the primary composition of the Snake River Plain upper and lower crust, respectively (5). As a part of the Snake River Plain bimodal silicic-basaltic volcanic sequence, the crustal composition beneath the Yellowstone caldera is likely similar. From laboratory experiments with a global compilation dataset (45), mafic granulite has an average  $V_P$  of  $\sim 6.8$  km/s and a temperature coefficient of  $-0.52 \times 10^3$  km/s/ $^\circ\text{C}$ . Assuming the mantle plume is the dominant heat source and perfectly transfers the heat into the lowermost crust, we can then use the excess temperature of the plume to assess the velocity reduction in the lower crust. Previous studies have suggested the excess temperature of the Yellowstone plume to be 55-120 K (2, 46). Using this value together with the temperature coefficient of mafic granulite gives a  $V_P$  decrease of 0.029-0.062 km/s, corresponding to a 0.4-0.9% velocity reduction. Thus, the composition and the temperature variations are not likely to be large enough to explain the high  $V_P$  reductions observed in the lower crust and require an additional source, such as partial melts, to account for the observation. For the upper-crustal rhyolitic reservoir, the melt fraction calculation uses a relation that has taken in situ high temperatures into account (13).

### Volume estimate of crustal magma bodies

Quantifying the uncertainties of tomographic inversions is challenging. In this study, we tend to be conservative and provide a lower-bound estimate, e.g. 5%  $V_P$  reduction. We then discretize the model space into 8 km<sup>3</sup> cubes and integrate those within a 5% contour of  $V_P$  reduction to obtain the total volumes. Note that the bottom of the lower crustal reservoir is fixed at the Moho depth of 45 km (26) for calculation because of its relatively poorer resolution (Fig. S6). Different volume estimates using different choices of  $V_P$  reduction are shown in Fig. S7. Based on the previous section, temperature anomalies could contribute up to 1% of the  $V_P$  reduction. Moreover, thermal considerations suggest that the

volume of basaltic magma parental to the rhyolite will be at least three to five times greater than that of derivative silicic magma (27). Because choosing a  $V_P$  reduction greater than 6% results in a volume ratio smaller than 3 (Fig. S7C), we therefore narrow the possible range of  $V_P$  reduction to 2-6 %. The range then results in volumes of 8,000-18,000 km<sup>3</sup> for the upper crustal reservoir and 30,000-116,000 km<sup>3</sup> for lower crustal one, respectively. The volume gradient with respect to the  $V_P$  reduction also reveals that the boundary of upper crustal reservoir is much sharper than that of the lower crustal reservoir (Figure S7A).

#### Melt fraction of crustal magma bodies

A relationship between absolute  $P$ -wave and  $S$ -wave velocities with respect to various porosities with melt and fluid saturations has been determined by (13) based on an assumption of a fluid-saturated porous material consisting of granite and a mixture of rhyolite melt and water and CO<sub>2</sub> at a temperature of 800°C and pressure at 5 km depth (0.1 GPa) for an upper-crust rhyolitic magma body beneath the Yellowstone caldera. Following this relation, we averaged the  $V_P$  over the volume of the upper-crustal LVB and get 5.21 km/s. Introducing this value into the relation gives ~9% porosity (i.e., melt fraction). Note that this relation assumes all pore fluids are in the equilibrium state throughout the pore space. Theoretically, we can derive a similar relation for the lower-crustal magma reservoir by replacing rhyolite with basalt and granite with granulite. However, this relation would rely on absolute velocity information, which is inherently lost when demeaned relative travel times of the teleseismic data are used. So for the structures mainly constrained by the teleseismic data, e.g. for depths greater than 20 km based on our tests (Fig. S4, S5, S6), this relation may not be applicable. Thus, a melt-fraction relation with respect to the  $V_P$  perturbation for the upper mantle peridotite-basalt-melt system is taken (47, 48), by assuming similar elastic properties between the lower crust and the uppermost mantle beneath the Yellowstone caldera. This assumption is approximate but likely close to reality because of the high velocity and dense underplated layers that have been reported for the Snake River Plain (5, 33). According to different partial derivatives with different shapes and states of melt inclusions (Table S2), and given an average  $V_P$  reduction of 6.56% calculated over the  $V_P = -5\%$  contour of the lower-crustal LVB, we estimate a 2-5% melt fraction (Table S2). Because the Yellowstone magmatic system inflates and deflates at rates of ~2-3 cm/yr (5), i.e., based on historic GPS measurements, and the extraordinary thermal and CO<sub>2</sub> degassing properties require a contribution from the deep basaltic reservoir (7, 8), the relaxed state that represents the pressure equilibrium inclusions with high connectivity and mobility of melts is more preferable in this case. Thus, using the  $V_P$  reduction derivatives of 3.6% (Table S2) gives us a ~2% melt fraction and a potential melt volume of 900 km<sup>3</sup>. Since the existence of water and gas bubbles can also lower the seismic velocity (13), these estimates should be regarded as an upper bound for melt fraction.

#### CO<sub>2</sub> depletion time of crustal magma bodies

We convert the daily CO<sub>2</sub> surface emission rate (45,000 ± 16,000 tons/day) into an annual emission rate of 1.642×10<sup>10</sup> kg/yr. Assuming that 50% of the degassed output originates from the subsurface magma, as estimated by carbon and helium isotopes (28), the annual emission rate of CO<sub>2</sub> contributed from the magma is 8.21×10<sup>9</sup> kg/yr. Given the parameters listed in Table S3, the total CO<sub>2</sub> mass dissolved within a magma reservoir can then be calculated as the following:

$$M_{CO_2} = M_{melt} \times r = D_{melt} \times V_{melt} \times r \quad (S3)$$

where  $M_{melt}$  and  $M_{CO_2}$  are the mass of the melts and the dissolved  $CO_2$ . Replacing  $M_{melt}$  with the product of density  $D_{melt}$ , and volume  $V_{melt}$ , and given the  $CO_2$  abundance,  $r$ , we obtain estimates of the current dissolved  $CO_2$  mass of  $8.4 \times 10^{11}$  kg and  $2.7 \times 10^{13}$  kg for the upper- and lower-crustal LVBs, respectively. The summed  $CO_2$  mass of the two LVBs divided by the annual emission rate of magma-contributed  $CO_2$  then results in a  $\sim 3,300$  year  $CO_2$  depletion time assuming no replenishment from the mantle source.

The high intensity of the Yellowstone hydrothermal system has been suggested to be active for  $\sim 15,000$  years or longer (29). If we assume the entire magma reservoir is a consequence of the solidification of previous melts, the onset time of  $CO_2$  degassing can then be estimated by replacing the melt volume (e.g. 9%) with the solidified portion of the magma body volume (e.g. 91%) in Eq. S3. Similar calculations have been previously done for the rhyolitic magma reservoir (6, 13) and gave  $\sim 1000$  years, which is far less than the 15,000 years for the age of the hydrothermal system and therefore led to a claim of additional basaltic input (6, 7, 13). Introducing the magma body volume obtained in this study, we obtain 1,100 and 160,000 years ago for the  $CO_2$  onset time for the rhyolitic and basaltic reservoirs, respectively. The rhyolite estimate agrees well with those in previous studies, and the basalt estimate gives a time an order of magnitude longer than  $\sim 15,000$  years, and between the occurrence of the youngest rhyolite flow (70 ka) and the caldera forming eruption (0.64 Ma) (1). This implies that the imaged lower crustal basaltic reservoir is sufficient to sustain the overlying rhyolitic reservoir and to supply the large discharge of  $CO_2$ , although whether the  $CO_2$  from the basaltic reservoir always goes through the overlying rhyolitic reservoir or in part through some direct path to the surface is unknown. Finally, we point out that the lateral migration of gas and potential ground water level change after the last glaciation termination at  $\sim 14,000$  years (29) are also variables that hinder the calculation from being more detailed.

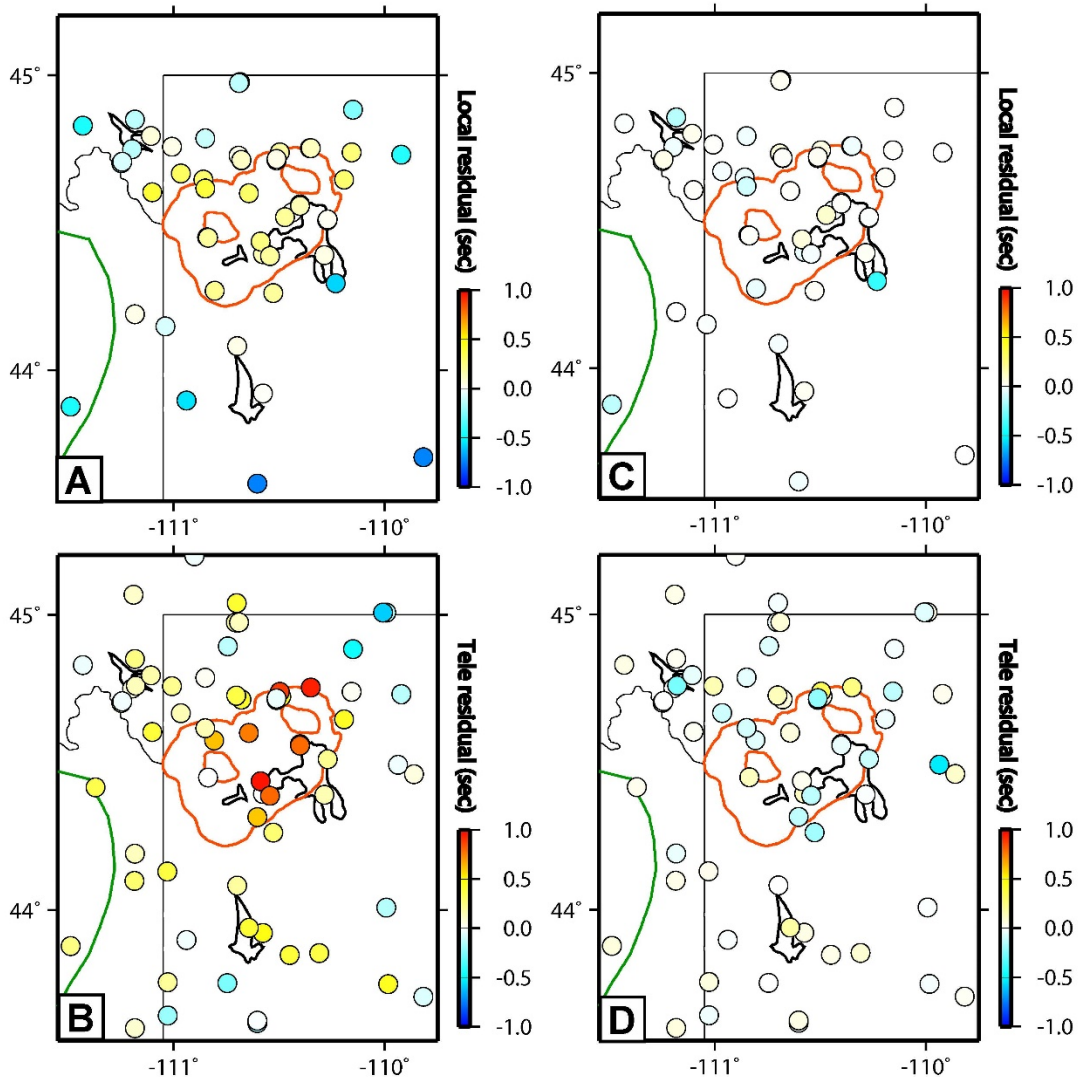


**Fig. S1. Averaged seismic station *P*-wave time residual map before and after the joint inversion.** Initial residuals of local earthquake arrival times (A) and teleseismic differential times (B) before inversion, and final residuals of local earthquake arrival times (C) and teleseismic differential times (D) after the inversion.

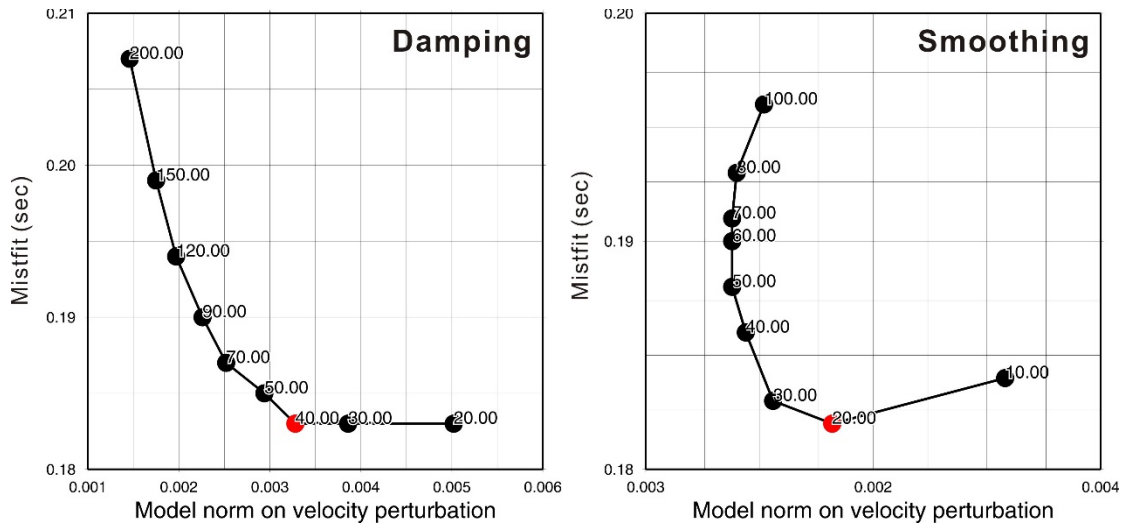


**Fig. S2 Trade-off curve tests for damping and smoothing parameters.** The labeled black dots are different damping and smoothing values we tested, and the labeled red dots are the final choices used for the inversion.

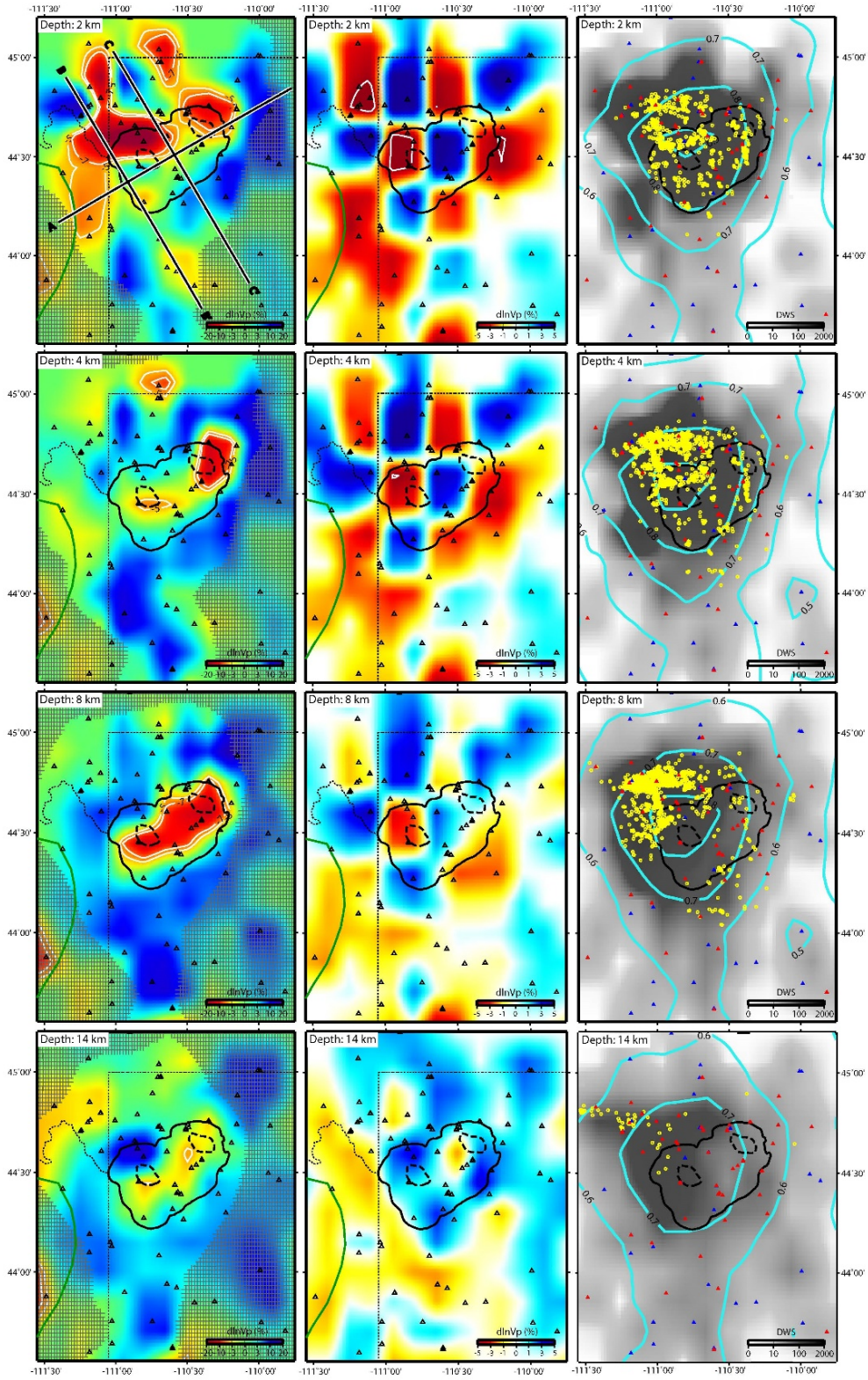


**Fig. S3 Inverted  $P$ -wave velocity model, checkerboard test, and derivative weighted sum (DWS) at each depth.**

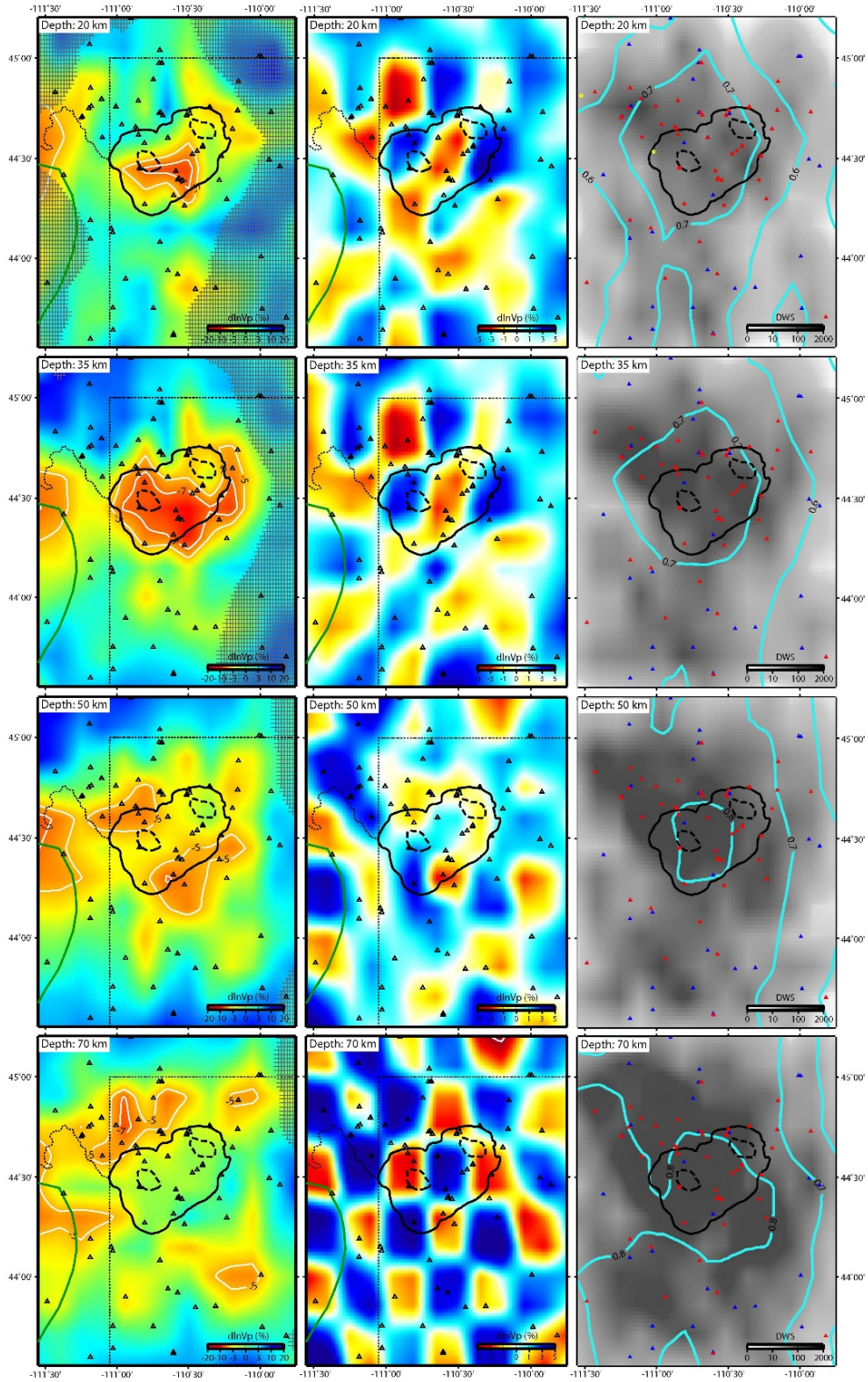


**Fig. S3 Inverted  $P$ -wave velocity model, checkerboard test, and derivative weighted sum (DWS) at each depth (continued).**

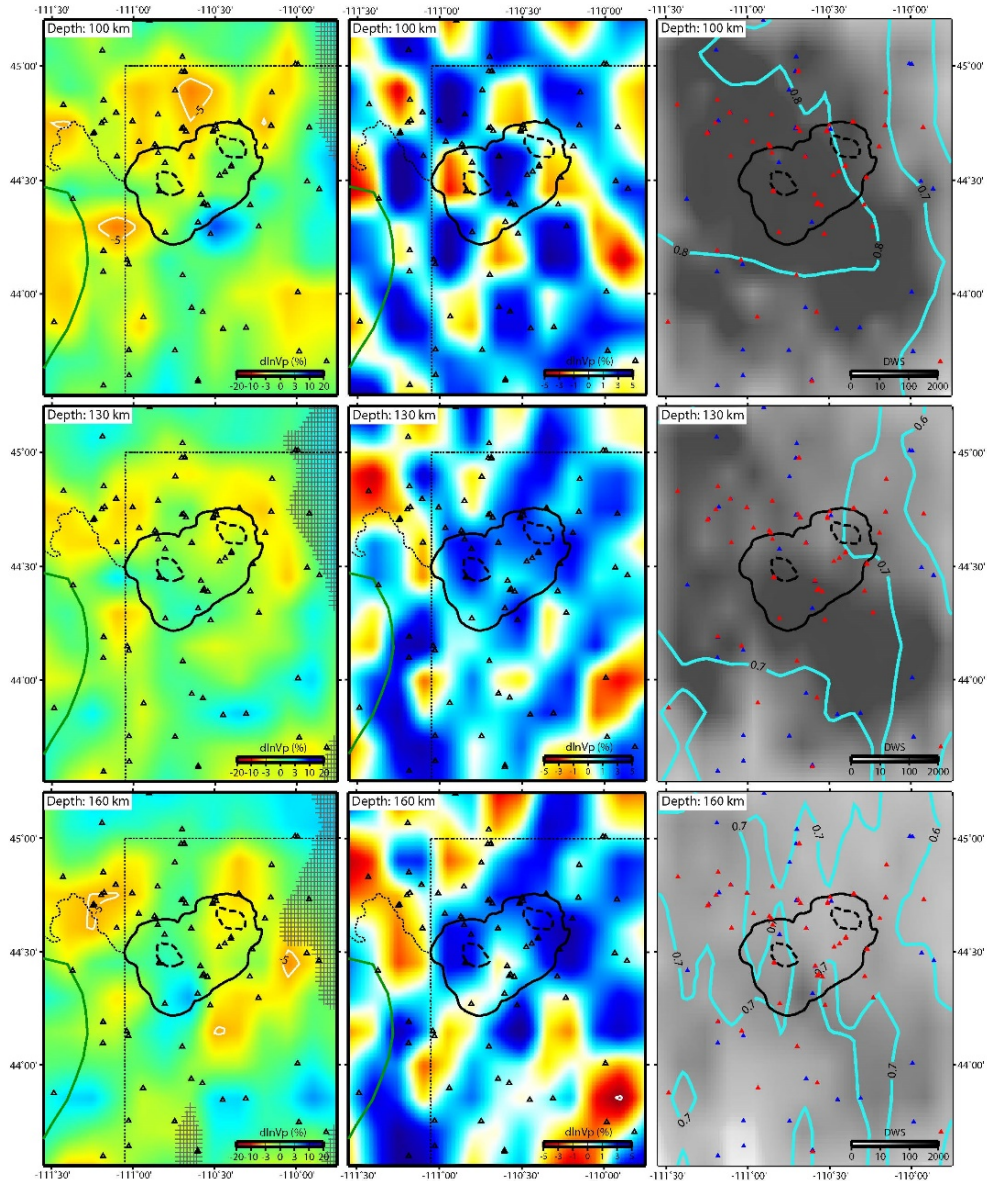


**Fig. S3 Inverted  $P$ -wave velocity model, checkerboard test, and derivative weighted sum (DWS) at each depth (continued).** Black thick solid, dashed, and thin dotted lines denote the Yellowstone caldera, resurgent domes in the caldera, and the state borders, respectively. Green lines represent the tectonic division of the Eastern Snake River Plain. The locations of cross-sections are shown on the depth slice of 2 km. Stations are indicated as black triangles in the left and middle columns. On the right column, red and blue triangles represent the stations that record and do not record the local earthquakes, respectively. Note that teleseismic earthquakes are recorded by both the red and blue stations. Yellow circles and cyan contours show the local earthquake distribution and the translated resolvability,  $R$ , from Eq. S1 at different depths.

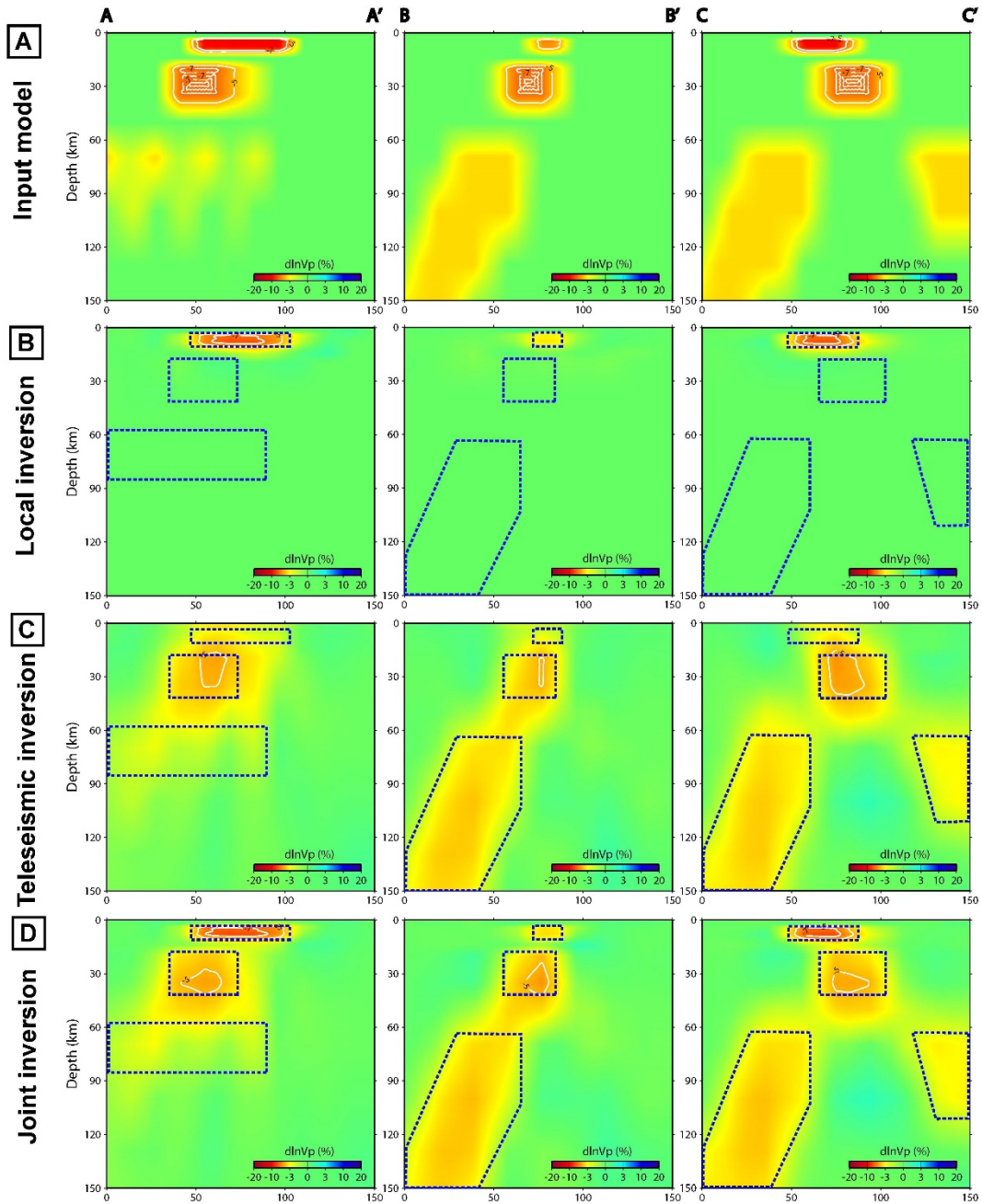


**Fig. S4 Characteristic model test for local earthquake, teleseismic, and joint inversions.** The input model (A) and the recovered images from the inversion with local data alone (B), with teleseismic data alone (C), and jointly with local and teleseismic data together (D). Blue dotted lines denote the approximate boundaries of input LVAs.

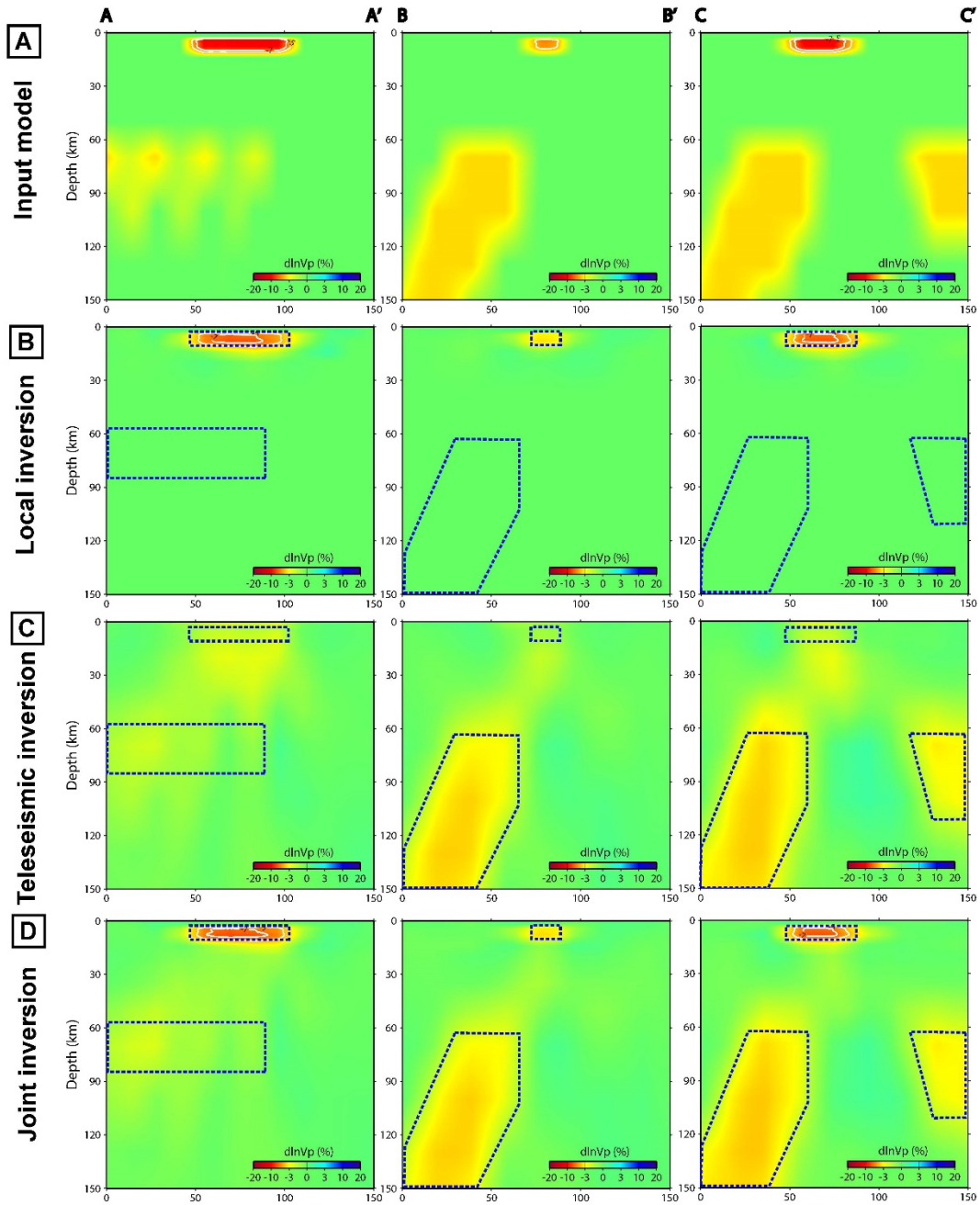


**Fig. S5 Characteristic model test without the lower-crustal anomaly for local earthquake, teleseismic, and joint inversions.** The input model (A) and the recovered images from the inversion with local data alone (B), with teleseismic data alone (C), and jointly with local and teleseismic data together (D). Blue dotted lines denote the approximate boundaries of input LVAs.

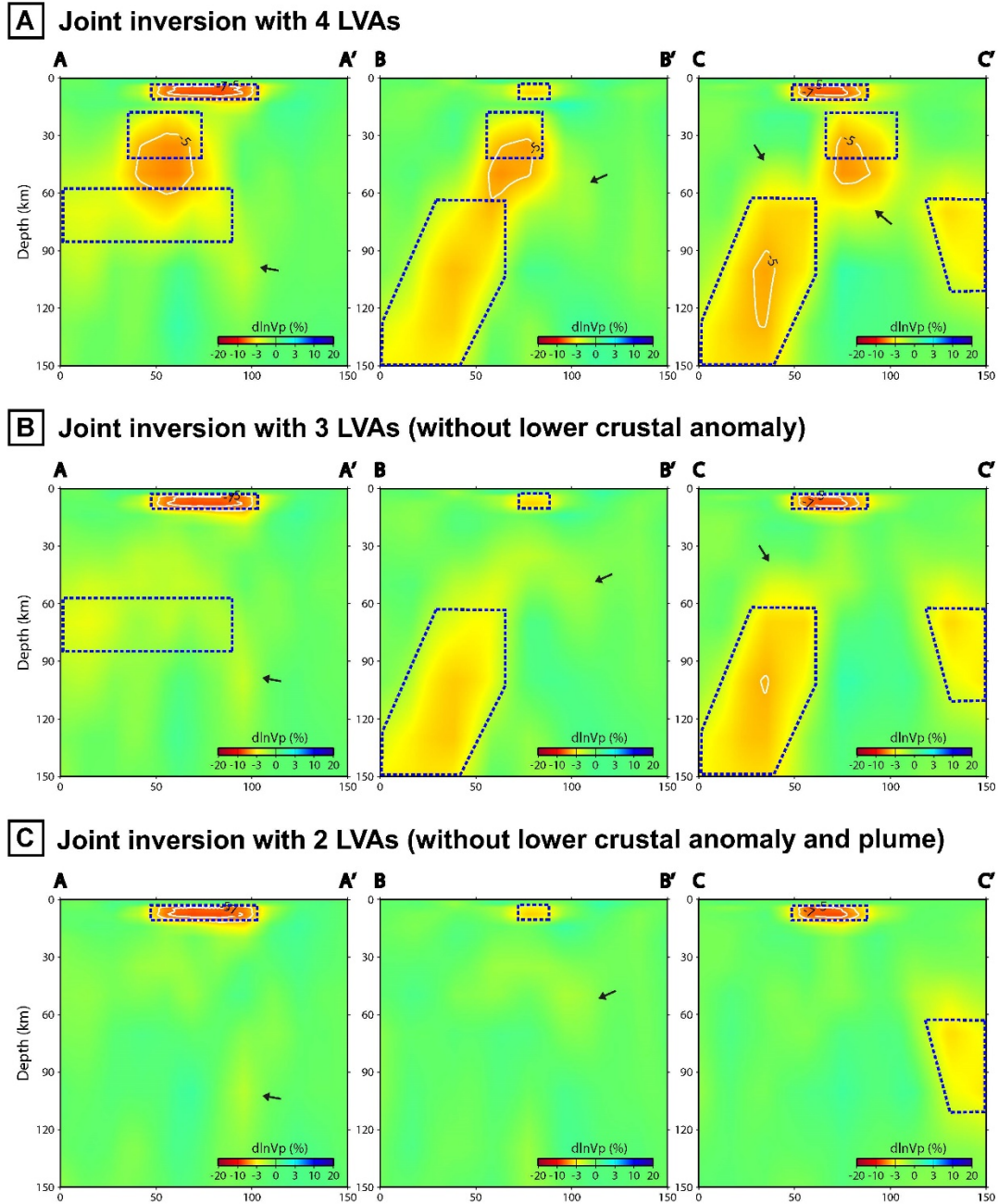


**Fig. S6 Characteristic model test with noise level of 0.13 s.** Testing the smearing with noise for a model with (A) 4 LVAs, (B) with 3 LVAs (without lower crustal anomaly), and (C) with 2 LVAs (without lower crustal anomaly and plume). All results are by joint inversion of local earthquake and teleseismic data. Blue dotted lines denote the approximate boundaries of input LVAs shown in Fig. S4A. Black arrows indicate the smearing artifacts.

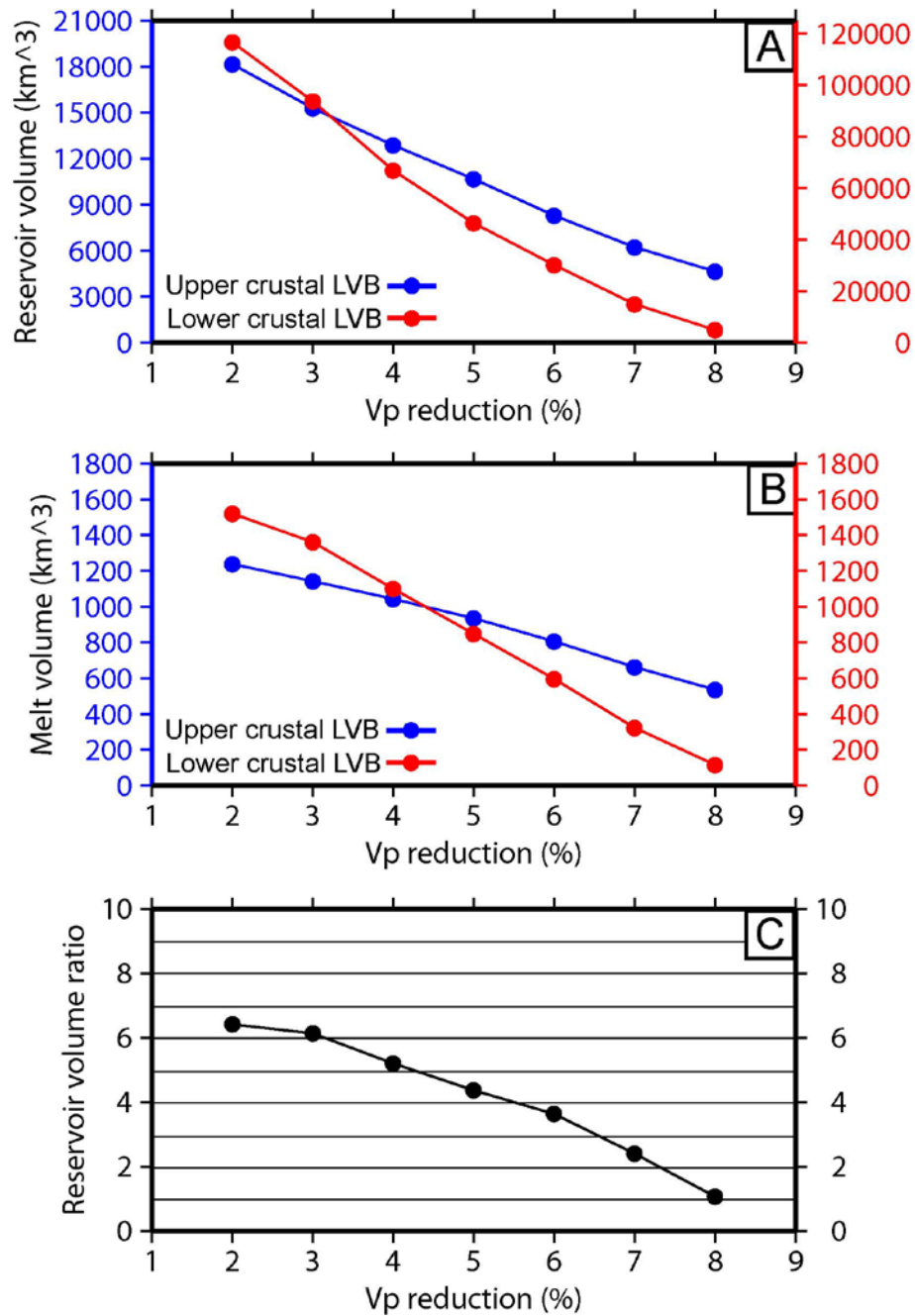


**Fig. S7 Volume estimate and ratio with different  $V_P$  reduction (%).** (A) Estimates of magma reservoir volume; (B) Estimates of partial melt volume; and (C) Ratio between upper and lower crustal magma reservoir volume.

**Table S1. Initial 1-D *P*-wave velocity model used in this study.**

<b>Model nodes depth (km)</b>	<b><i>P</i>-wave at velocity (km/s)</b>
-10.0	3.700
-4.0	3.800
2.0	5.240
4.0	5.420
8.0	5.650
14.0	6.120
20.0	6.300
35.0	6.500
50.0	7.500
70.0	8.015
100.0	8.048
130.0	8.080
160.0	8.156

**Table S2. Reference partial derivatives of  $P$ -wave velocity with respect to melt fraction.** Velocity reduction derivatives are in percentage. The unrelaxed state and the relaxed state represent the conditions of isolated inclusions and pressure-equalized inclusions.  $V_p$ ,  $P$ -wave velocity (km/s); F, melt fraction (%). Numbers in parentheses denote references.

$-\partial \ln V_p / \partial F$	Melt inclusion description
1.23	Unrelaxed state, dihedral angle typical (48)
2.9	Unrelaxed state, organized cusped shape (47)
3.6	Relaxed state, organized cusped shape (47)

**Table S3. Geophysical and geochemical parameters used for the CO<sub>2</sub> calculation.**  
 Numbers in parentheses denote references.

<b>Magma type</b>	<b>Density (kg/km<sup>3</sup>)</b>	<b>CO<sub>2</sub> abundance in the melts (ppm)</b>	<b>Reservoir volume (km<sup>3</sup>)</b>	<b>Melt volume (km<sup>3</sup>)</b>
Basalt	2.9×10 <sup>12</sup> (28)	10,000 (6)	46,000 (*)	900 (*)
Rhyolite	2.2×10 <sup>12</sup> (13)	400 (6)	10,000 (*)	900 (*)

\* derived from this study.

## References

1. R. L. Christiansen, *U.S. Geol. Surv. Prof. Pap.* 729-G, 145 (2001).
2. R. B. Smith, M. Jordan, B. Steinberger, C. M. Puskas, J. Farrell, G. P. Waite, S. Husen, W. L. Chang, R. O'Connell, Geodynamics of the Yellowstone hotspot and mantle plume: Seismic and GPS imaging, kinematics, and mantle flow. *J. Volcanol. Geotherm. Res.* **188**, 26–56 (2009). [doi:10.1016/j.jvolgeores.2009.08.020](https://doi.org/10.1016/j.jvolgeores.2009.08.020)
3. J. Farrell, R. B. Smith, S. Husen, T. Diehl, Tomography from 26 years of seismicity revealing that the spatial extent of the Yellowstone crustal magma reservoir extends well beyond the Yellowstone caldera. *Geophys. Res. Lett.* **41**, 3068–3073 (2014).  
[doi:10.1002/2014GL059588](https://doi.org/10.1002/2014GL059588)
4. W. L. Chang, R. B. Smith, C. Wicks, J. M. Farrell, C. M. Puskas, Accelerated uplift and magmatic intrusion of the Yellowstone caldera, 2004 to 2006. *Science* **318**, 952–956 (2007). [Medline doi:10.1126/science.1146842](https://doi.org/10.1126/science.1146842)
5. K. R. DeNosaquo, R. B. Smith, A. R. Lowry, Density and lithospheric strength models of the Yellowstone–Snake River Plain volcanic system from gravity and heat flow data. *J. Volcanol. Geotherm. Res.* **188**, 108–127 (2009). [doi:10.1016/j.jvolgeores.2009.08.006](https://doi.org/10.1016/j.jvolgeores.2009.08.006)
6. J. B. Lowenstern, S. Hurwitz, Monitoring a supervolcano in repose: Heat and volatile flux at the Yellowstone caldera. *Elements* **4**, 35–40 (2008). [doi:10.2113/GSELEMENTS.4.1.35](https://doi.org/10.2113/GSELEMENTS.4.1.35)
7. S. Hurwitz, J. B. Lowenstern, Dynamics of the Yellowstone hydrothermal system. *Rev. Geophys.* **52**, 375–411 (2014). [doi:10.1002/2014RG000452](https://doi.org/10.1002/2014RG000452)
8. H. Yuan, K. Dueker, Teleseismic *P*-wave tomogram of the Yellowstone plume. *Geophys. Res. Lett.* **32**, L07304 (2005). [doi:10.1029/2004GL022056](https://doi.org/10.1029/2004GL022056)

9. M. Xue, R. M. Allen, Mantle structure beneath the western United States and its implications for convection processes. *J. Geophys. Res.* **115**, B07303 (2010). [doi:10.1029/2008JB006079](https://doi.org/10.1029/2008JB006079)
10. M. Obrebski, R. M. Allen, F. Pollitz, S. H. Hung, Lithosphere-asthenosphere interaction beneath the western United States from the joint inversion of body-wave traveltimes and surface-wave phase velocities. *Geophys. J. Int.* **185**, 1003–1021 (2011).  
[doi:10.1111/j.1365-246X.2011.04990.x](https://doi.org/10.1111/j.1365-246X.2011.04990.x)
11. B. Schmandt, K. Dueker, E. Humphreys, S. Hansen, Hot mantle upwelling across the 660 beneath Yellowstone. *Earth Planet. Sci. Lett.* **331–332**, 224–236 (2012).  
[doi:10.1016/j.epsl.2012.03.025](https://doi.org/10.1016/j.epsl.2012.03.025)
12. S. Husen, R. B. Smith, G. P. Waite, Evidence for gas and magmatic sources beneath the Yellowstone volcanic field from seismic tomographic imaging. *J. Volcanol. Geotherm. Res.* **131**, 397–410 (2004). [doi:10.1016/S0377-0273\(03\)00416-5](https://doi.org/10.1016/S0377-0273(03)00416-5)
13. R. Chu, D. V. Helmberger, D. Sun, J. M. Jackson, L. Zhu, Mushy magma beneath Yellowstone. *Geophys. Res. Lett.* **37**, L01306 (2010). [doi:10.1029/2009GL041656](https://doi.org/10.1029/2009GL041656)
14. M. Paulatto, C. Annen, T. J. Henstock, E. Kiddle, T. A. Minshull, R. S. J. Sparks, B. Voight, Magma chamber properties from integrated seismic tomography and thermal modeling at Montserrat. *Geochem. Geophys. Geosyst.* **13**, Q01014 (2012).  
[doi:10.1029/2011GC003892](https://doi.org/10.1029/2011GC003892)
15. M. A. Mitchell, R. S. White, S. Roecker, T. Greenfield, Tomographic image of melt storage beneath Askja Volcano, Iceland using local microseismicity. *Geophys. Res. Lett.* **40**, 5040–5046 (2013). [doi:10.1002/grl.50899](https://doi.org/10.1002/grl.50899)

16. M. West, W. Menke, M. Tolstoy, S. Webb, R. Sohn, Magma storage beneath Axial volcano on the Juan de Fuca mid-ocean ridge. *Nature* **413**, 833–836 (2001). [Medline](#)  
[doi:10.1038/35101581](https://doi.org/10.1038/35101581)
17. E. M. Syracuse, C. H. Thurber, C. J. Wolfe, P. G. Okubo, J. H. Foster, B. A. Brooks, High-resolution locations of triggered earthquakes and tomographic imaging of Kilauea Volcano's south flank. *J. Geophys. Res.* **115**, B10310 (2010). [doi:10.1029/2010JB007554](https://doi.org/10.1029/2010JB007554)
18. G. P. Waite, S. C. Moran, VP Structure of Mount St. Helens, Washington, USA, imaged with local earthquake tomography. *J. Volcanol. Geotherm. Res.* **182**, 113–122 (2009).  
[doi:10.1016/j.jvolgeores.2009.02.009](https://doi.org/10.1016/j.jvolgeores.2009.02.009)
19. I. Koulakov, E. I. Gordeev, N. L. Dobretsov, V. A. Vernikovskiy, S. Senyukov, A. Jakovlev, K. Jaxybulatov, Rapid changes in magma storage beneath the Klyuchevskoy group of volcanoes inferred from time-dependent seismic tomography. *J. Volcanol. Geotherm. Res.* **263**, 75–91 (2013). [doi:10.1016/j.jvolgeores.2012.10.014](https://doi.org/10.1016/j.jvolgeores.2012.10.014)
20. K. J. Seats, J. F. Lawrence, The seismic structure beneath the Yellowstone Volcano Field from ambient seismic noise. *Geophys. Res. Lett.* **41**, 8277–8282 (2014).  
[doi:10.1002/2014GL061913](https://doi.org/10.1002/2014GL061913)
21. S. W. Roecker, T. M. Sabitova, L. P. Vinnik, Y. A. Burmakov, M. I. Golvanov, R. Mamatkanova, L. Munirova, Three-dimensional elastic wave velocity structure of the western and central Tien Shan. *J. Geophys. Res.* **98**, 15779 (1993).  
[doi:10.1029/93JB01560](https://doi.org/10.1029/93JB01560)

22. D. Zhao, A. Hasegawa, H. Kanamori, Deep structure of Japan subduction zone as derived from local, regional, and teleseismic events. *J. Geophys. Res.* **99**, 22313–22329 (1994).  
[doi:10.1029/94JB01149](https://doi.org/10.1029/94JB01149)
23. H.-H. Huang, Y.-M. Wu, X. Song, C.-H. Chang, H. Kuo-Chen, S.-J. Lee, Investigating the lithospheric velocity structures beneath the Taiwan region by nonlinear joint inversion of local and teleseismic *P* wave data: Slab continuity and deflection. *Geophys. Res. Lett.* **41**, (2014). [doi:10.1002/2014GL061115](https://doi.org/10.1002/2014GL061115)
24. B. Schmandt, F. C. Lin, *P* and *S* wave tomography of the mantle beneath the United States. *Geophys. Res. Lett.* **41**, 6342–6349 (2014). [doi:10.1002/2014GL061231](https://doi.org/10.1002/2014GL061231)
25. See supplementary materials on *Science* Online.
26. W. Shen, M. H. Ritzwoller, V. Schulte-Pelkum, A 3-D model of the crust and uppermost mantle beneath the Central and Western US by joint inversion of receiver functions and surface wave dispersion. *J. Geophys. Res.* **118**, 262–276 (2013).  
[doi:10.1029/2012JB009602](https://doi.org/10.1029/2012JB009602)
27. S. M. White, J. A. Crisp, F. J. Spera, Long-term volumetric eruption rates and magma budgets. *Geochem. Geophys. Geosyst.* **7**, Q03010 (2006). [doi:10.1029/2005GC001002](https://doi.org/10.1029/2005GC001002)
28. C. Werner, S. Brantley, CO<sub>2</sub> emissions from the Yellowstone volcanic system. *Geochem. Geophys. Geosyst.* **4**, 1061 (2003). [doi:10.1029/2002GC000473](https://doi.org/10.1029/2002GC000473)
29. R. O. Fournier, Geochemistry and dynamics of the Yellowstone National Park hydrothermal system. *Annu. Rev. Earth Planet. Sci.* **17**, 13–53 (1989).  
[doi:10.1146/annurev.ea.17.050189.000305](https://doi.org/10.1146/annurev.ea.17.050189.000305)

30. K. Jaxybulatov, N. M. Shapiro, I. Koulakov, A. Mordret, M. Landès, C. Sens-Schönfelder, A large magmatic sill complex beneath the Toba caldera. *Science* **346**, 617–619 (2014).  
[Medline doi:10.1126/science.1258582](#)
31. C. Annen, J. D. Blundy, R. S. J. Sparks, The genesis of intermediate and silicic magmas in deep crustal hot zones. *J. Petrol.* **47**, 505–539 (2006). [doi:10.1093/petrology/egi084](#)
32. A. Gudmundsson, Deflection of dykes into sills at discontinuities and magma-chamber formation. *Tectonophysics* **500**, 50–64 (2011). [doi:10.1016/j.tecto.2009.10.015](#)
33. J. W. Shervais, S. K. Vetter, B. B. Hanan, Layered mafic sill complex beneath the eastern Snake River Plain: Evidence from cyclic geochemical variations in basalt. *Geology* **34**, 365 (2006). [doi:10.1130/G22226.1](#)
34. Z. J. Xu, X. Song, Joint inversion for crustal and Pn velocities and Moho depth in Eastern Margin of the Tibetan Plateau. *Tectonophysics* **491**, 185–193 (2010).  
[doi:10.1016/j.tecto.2009.11.022](#)
35. H.-H. Huang, Z. Xu, Y.-M. Wu, X. Song, B.-S. Huang, N. L. Minh, First local seismic tomography for Red River shear zone, northern Vietnam: Stepwise inversion employing crustal P and Pn waves. *Tectonophysics* **584**, 230–239 (2013).  
[doi:10.1016/j.tecto.2012.03.030](#)
36. H. H. Huang, Y. M. Wu, X. Song, C. H. Chang, S. J. Lee, T. M. Chang, H. H. Hsieh, Joint  $V_p$  and  $V_s$  tomography of Taiwan: Implications for subduction-collision orogeny. *Earth Planet. Sci. Lett.* **392**, 177–191 (2014). [doi:10.1016/j.epsl.2014.02.026](#)
37. J. Um, C. Thurber, A fast algorithm for two-point seismic ray tracing. *Bull. Seismol. Soc. Am.* **77**, 972–986 (1987).

38. K. Koketsu, S. Sekine, Pseudo-bending method for three-dimensional seismic ray tracing in a spherical Earth with discontinuities. *Geophys. J. Int.* **132**, 339–346 (1998).  
[doi:10.1046/j.1365-246x.1998.00427.x](https://doi.org/10.1046/j.1365-246x.1998.00427.x)
39. B. L. N. Kennett, E. R. Engdahl, R. Buland, Constraints on seismic velocities in the Earth from traveltimes. *Geophys. J. Int.* **122**, 108–124 (1995).  
[doi:10.1111/j.1365-246X.1995.tb03540.x](https://doi.org/10.1111/j.1365-246X.1995.tb03540.x)
40. J. A. Snoke, J. C. Lahr, Locating earthquakes: At what distance can the Earth no longer be treated as flat? *Seismol. Res. Lett.* **72**, 538–541 (2001). [doi:10.1785/gssrl.72.5.538](https://doi.org/10.1785/gssrl.72.5.538)
41. C. A. Zelt, Lateral velocity resolution from three-dimensional seismic refraction data. *Geophys. J. Int.* **135**, 1101–1112 (1998). [doi:10.1046/j.1365-246X.1998.00695.x](https://doi.org/10.1046/j.1365-246X.1998.00695.x)
42. C. H. Thurber, D. Eberhart-Phillips, Local earthquake tomography with flexible gridding. *Comput. Geosci.* **25**, 809–818 (1999). [doi:10.1016/S0098-3004\(99\)00007-2](https://doi.org/10.1016/S0098-3004(99)00007-2)
43. J. Spetzler, R. Snieder, The Fresnel volume and transmitted waves. *Geophysics* **69**, 653–663 (2004). [doi:10.1190/1.1759451](https://doi.org/10.1190/1.1759451)
44. H. P. Crotwell, T. J. Owens, J. Ritsema, The TauP toolkit: Flexible seismic travel-time and ray-path utilities. *Seismol. Res. Lett.* **70**, 154–160 (1999). [doi:10.1785/gssrl.70.2.154](https://doi.org/10.1785/gssrl.70.2.154)
45. N. I. Christensen, W. D. Mooney, Seismic velocity structure and composition of the continental crust: A global view. *J. Geophys. Res.* **100**, 9761–9788 (1995).  
[doi:10.1029/95JB00259](https://doi.org/10.1029/95JB00259)
46. D. L. Schutt, K. Dueker, Temperature of the plume layer beneath the Yellowstone hotspot. *Geology* **36**, 623 (2008). [doi:10.1130/G24809A.1](https://doi.org/10.1130/G24809A.1)

47. W. C. Hammond, E. D. Humphreys, Upper mantle seismic wave velocity: Effects of realistic partial melt geometries. *J. Geophys. Res.* **105**, 10975 (2000). [doi:10.1029/2000JB900041](https://doi.org/10.1029/2000JB900041)
48. A. Kreuzmann, H. Schmeling, A. Junge, T. Ruedas, G. Marquart, I. Th. Bjarnason, Temperature and melting of a ridge-centred plume with application to Iceland. Part II: Predictions for electromagnetic and seismic observables. *Geophys. J. Int.* **159**, 1097–1111 (2004). [doi:10.1111/j.1365-246X.2004.02397.x](https://doi.org/10.1111/j.1365-246X.2004.02397.x)